Competing effects of collisional ionization and radiative cooling in inertially confined plasmas

N. C. Woolsey*
School of Mathematics and Physics, Queen's University of Belfast, Belfast, BT7 1NN, Northern Ireland

B. A. Hammel, C. J. Keane, C. A. Back, J. C. Moreno, and J. K. Nash
LLNL, University of California, P.O. Box 808, Livermore, California 94551

A. Calisti, C. Mossé, R. Stamm, and B. Talin
Centre St. Jérôme, Université Aix Marseille 1, PIIM, URA 773, Case 232, F-13397, Marseille 20, France

A. Asfaw and L. S. Klein
Department of Physics, Howard University, Washington, D.C. 20059

R. W. Lee
Department of Physics, University of California, Berkeley, California 94720-7300
(Received 1 December 1997)

We describe an experimental investigation, a detailed analysis of the Ar XVII $1s^2\ ^1S-1s3p\ ^1P$ (Heβ) line shape formed in a high-energy-density implosion, and report on one-dimensional radiation-hydrodynamics simulation of the implosion. In this experiment trace quantities of argon are doped into a lower-Z gas-filled core of a plastic microsphere. The dopant level is controlled to ensure that the Heβ transition is optically thin and easily observable. Then the observed line shape is used to derive electron temperatures (T_e) and electron densities (n_e). The high-energy density plasma, with T_e approaching 1 keV and $n_e = 10^{24}$ cm^{-3}, is created by placing the microsphere in a gold cylindrical enclosure, the interior of which is directly irradiated by a high-energy laser; the x rays produced by this laser-gold interaction indirectly implode the microsphere. Central to the interpretation of the hydrodynamics of the implosions is the characterization and understanding of the formation of these plasmas. To develop an understanding of the plasma and its temporal evolution, time-resolved T_e and n_e measurements are extracted using techniques that are independent of the plasma hydrodynamics. Comparing spectroscopic diagnostics with measurements derived from other diagnostic methods, we find the spectroscopic measurements to be reliable and further we find that the experiment-to-experiment comparison shows that these implosions are reproducible. [S1063-651X(98)05504-4]

PACS number(s): 52.25.Nr, 52.50.Lp, 52.58.Ns

I. INTRODUCTION

When a plastic microsphere is engulfed in a soft-x-ray radiation field the surface layer is strongly heated. This layer is ionized, expands, and moves outward compressing the interior; as the radiation field continues to heat the microsphere a shock wave and inward convergence of the shell results. Gas placed in the interior of the microsphere, for example, deuterium, is compressed and heated. During compression the gas is collisionally ionized; temperatures may be sufficient to highly ionize medium-Z dopants such as argon. In these experiments argon is added to the gas fill in trace quantities to enable spectroscopic measurements of the interior conditions and to enable basic spectroscopic research at high-energy density. Of particular interest are the line shapes of Stark-broadened lines of highly ionized Ar such as the Ar XVII $1s^2\ ^1S-1s3p\ ^1P$ (Ar Heβ) transition centered at 3.365 Å and the Ar XVIII 1-3 (Ar Lyβ) transition centered at 3.150 Å, which are used to determine the electron temperature (T_e) and electron density (n_e).

The high-energy-density conditions in an imploded core are of fundamental interest to atomic energy-level population kinetics, electron thermal conduction, radiation energy flow, and spectral line formation and of practical interest to inertial confinement fusion (ICF) research and astrophysics. It is critical to ICF to understand the time dependence of the core conditions. The data presented here demonstrate that accurate T_e and n_e measurements suitable for comparison to hydrodynamic simulation can be obtained from an ICF environment. We are particularly interested in the formation of inertially confined plasmas as a spectroscopic source and the effects the plasma may have on spectral line formation [1]. Indeed, ICF-type plasmas are complex, requiring careful experimental measurements; emission spectroscopy is one of the few techniques capable of providing time-resolved details of an inertially confined core [2–4]. Recently, we have shown that high-quality spectroscopic data can be obtained and analyzed to produce the time-dependent spatially averaged $T_e(t)$ and $n_e(t)$ of an imploding core; as the data are independent of hydrodynamic modeling, they can be compared with hydrodynamic simulations [2,3]. Thus, in the following, we explore the dynamics of an imploding core with spectroscopic techniques and hydrodynamic modeling as well as investigating the detailed Ar Heβ line shape.

Intense speculation on the role of ion dynamics at high-

*Electronic address: n.woolsey@qub.ac.uk

 © 1998 The American Physical Society

energy density [1,4–9] has centered on the absence of a local intensity minimum, or dip, at the line center of the Ar Heβ line-center in experiment. This dip is predicted by standard, quasistatic ion-broadening line-shape theory. We stress that there are a number of plausible explanations for the difference between experiment and theory. First, density gradients may exist in the imploded core and emission from lower-density regions may fill in the intensity dip in the line shape emitted from the denser regions of the core. Second, Li-like dielectronic satellites that lie to the low-energy side of the Ar Heβ transition may modify the line shape; for example, if temperatures are low enough the satellites will dominate the line profile. Third, if aspects of the core hydrodynamics are found not to influence the spectral line shapes, a modification to the standard quasistatic treatment of the ions to include a nonstationary ion-emitter interaction (i.e., ion dynamics) may be required. Including ion dynamics will improve agreement with experiment [1]. Determining T_e and n_e spatial gradients and the average T_e requires knowledge of the implosion hydrodynamics, whereas ion dynamic effects may be explored by replacing light elements (i.e., D_2) in the core with a heavier gas fill such as neon. Replacing the fill with a higher-Z gas, in effect, slows the ion motion, due to the increase in mass, slowing the ion field fluctuation rate. Then the dip at the Ar Heβ line center should be recovered. Again, the hydrodynamics of the implosion must be well understood. The implosion dynamics of these higher-Z gas-filled microspheres are particularly interesting as competing processes of radiative cooling may dominate collisional ionization in the plasma.

In the following we discuss the detailed spectroscopy of an implosion and explore the hydrodynamic simulation of the dynamics of indirectly driven inertially confined experiments. In Sec. II we present a detailed description of the experiment, the data reduction, and the data analysis procedures. The spectroscopic analysis follows two methods. First, detailed calculations of the Heβ and Li-like dielectronic satellites $2l3l'$ and $3l3l'$ composite line shapes are compared to experimental measurements to give T_e and n_e. In the second approach we use a more commonly used method: The line intensity ratios of Lyβ and Heβ are used to find T_e, while the full widths at half maximum (FWHMs) of the Heβ and Lyβ transitions are used to derive n_e. The implosion data obtained from a D_2-filled microsphere are described in Sec. III, while data from a series of experiments are used to prove that these inertially confined plasmas are created reliably and reproducibly. The D_2 data are then compared with results from similar experiments with argon-doped deuterated methane (CD_4), nitrogen (N_2), and neon (Ne) as the gas fill. These spectra illustrate that changing the fill gases significantly alters the implosion.

Motivated by the need to understand the dynamics of imploding microspheres, computer simulations are described in Sec. IV. Here one-dimensional radiation-hydrodynamic simulations of the implosion D_2 experiments are presented and are found to broadly represent the T_e and n_e data. The simulation model is extended to simulate the CD_4, N_2, and Ne experiments, finding that the increase in average atomic number $\langle Z \rangle$ considerably alters the implosion.

The experimental and hydrodynamic modeling results are compared in Sec. V. Finally, the sum of these efforts is to prove that an indirectly imploded, inertially confined D_2 plasma is a unique and useful spectroscopic source. Further, we will prove that this source allows the measurement of the Ar Heβ line shape, which could include the possibility of measuring ion dynamic effects in high-energy-density plasmas.

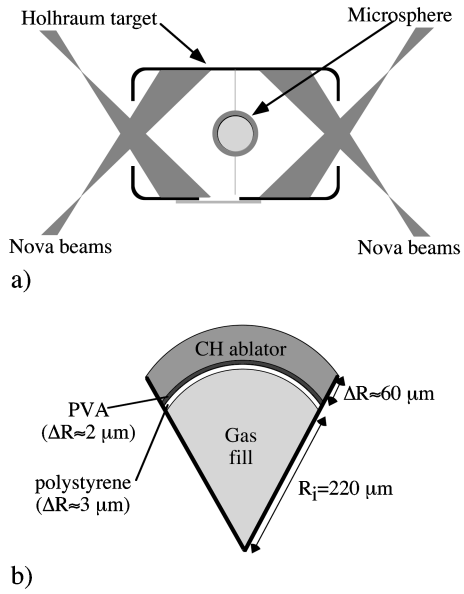

FIG. 1. Schematic of the (a) hohlraum target and (b) microsphere.

II. EXPERIMENTAL PROCEDURES

The experiments described were performed on the Nova laser [10] at the Lawrence Livermore National Laboratory. All the data are from indirectly driven implosions of gas-filled plastic microspheres. A soft-x-ray source is created by heating the interior of a millimeter-sized gold cylinder, a hohlraum target, with the Nova laser. The radiation source heats the outer surface of the microsphere that is placed at the hohlraum target center. This radiation causes ablation of the outer plastic shell driving an inward compression, as the interior implodes the fill gas is heated, compressed, and ionized. At sufficient temperatures the argon dopant is ionized to the K shell and its emission is recorded on x-ray crystal streak cameras, so that spectrally and temporally resolved measurements of the optically thin Ar Heβ transition are made.

A. Experiment technique

1. Target parameters

The hohlraum target is a gold cylinder 2.55 mm long and 1.6 mm in diameter with 25-μm-thick walls. Laser entrance holes (LEHs), 0.8 mm in diameter, are cut centrally in each end of the cylinder and diagnostic view holes are cut in the wall of the cylinder. The diagnostic view holes are patched with 12.5 μm of Be to reduce radiation loss, thus enhancing the symmetry of the radiation field at the hohlraum target center. The hohlraum target is illustrated in Fig. 1.

A microsphere, approximately 560 μm in diameter, is suspended at the hohlraum target center by a 400-Å-thick

TABLE I. Summary of the microsphere gas fills investigated. The first column refers to the figures in which data and simulations are shown.

Figure	Fill gas	Pressure (atm)	Dopant Ar (atm)	$\langle Z \rangle$	Average atomic mass	Laser energy (kJ)	Simulation energy (kJ)
			0.05			17.9	
2, 9(a)	D_2	50	0.1	1	2	19±2	16
			0.2			19.2	
			0.4			19.5	
5, 9(b)	CD_4	10	0.1	2	4	18.3	16
6(a), 9(c)	N_2	7	0.1	7	14	19.1	16
6(b), 9(d)	Ne	10	0.1	10	20	13.7	16

CH web. The web is supported by first splitting the hohlraum target and then sandwiching the web between the rejoined halves. Figure 1(b) illustrates the construction of the microsphere, which consists of a 2-μm-thick polystyrene shell of 220 μm internal radius overcoated with an impermeable 3-μm-thick polyvinyl alcohol (PVA) gas retention membrane. The outer shell is an approximately 56-μm-thick parylene-N ablator. The microsphere fill gases and shell construction are summarized in Tables I and II, respectively.

To ensure a reliable diagnostic, argon is introduced in trace amounts and optimized by considering three criteria: (i) the emission from *K*-shell argon must be observable; (ii) as line shapes are the principle T_e and n_e diagnostics, the lines of interest should be optically thin; and (iii) the concentration of argon should be low to ensure that the argon does not perturb the implosion hydrodynamics compared to an implosion with no argon. To assess the optical depth at the line center τ_0 we write

$$\tau_0 = F_{\mathrm{He}} F_{\mathrm{Ar}} n_e R_f \left(\frac{\pi e^2}{mc} f_{lu} \phi_0 \right), \tag{1}$$

where F_{Ar} is the Ar number by ion fraction, F_{He} is the fraction of Ar ions in the He-like ionization state, ρR_f is the peak areal mass density, and ϕ_0 is the emission profile at the line center. For the D_2-filled microspheres F_{Ar} is typically 0.1 at. %, while F_{He} is approximately 0.5 for the condition when the *K*-shell line will be observed and the ρR_f is measured from neutron yields to be ~ 6 mg/cm^2. The peak absorption cross section at the line center [the large parentheses in Eq. (1)] is calculated to be 2.3×10^{-19} cm^2 for Ar Heβ and 2.9×10^{-19} cm^2 for Ar Lyβ giving an optical depth of approximately 0.2 in each case for the D_2 gas fill [4].

TABLE II. Summary of the composition of the simulated microsphere.

	Composition	Density (g/cm^3)	Thickness (μm)	Zones	EOS	Atomic physics
core	Table I	Table I	220	50	ideal gas	NLTE
	polystyrene C_8H_8	1.06	2	8	ideal gas	NLTE
shell	PVA C_2H_4O	1.46	3	3	ideal gas	NLTE
	parylene-N C_8H_8	1.05	56	16	ideal gas	NLTE

2. Laser parameters

To create the x-ray drive ten synchronized Nova laser beams were used. The beams had a temporally square pulse shapes of 1 ns duration with ~ 2 kJ of energy per beam at a wavelength of 0.353 μm. Five laser beams enter the hohlraum target from each side in a cone with a half apex angle of 50° and $f/4.3$ optics. The beams were centered on the LEH and then defocused 1000 μm further from the LEH to form an irradiated annulus on the interior wall of the hohlraum target. The average irradiance in the annulus was approximately 2×10^{15} W/cm^2. The laser plasma formed at the hohlraum target wall effectively up-converts the laser radiation [11,12] to a radiation field that peaks at 230 eV [3]. This radiation field impinges on the outer plastic coating of the microsphere.

3. Instrumentation

The Ar emission from the microsphere core was diagnosed using x-ray instruments that were installed in 6-in. tubes [13]. Two x-ray streak-camera-based spectrometers [14] and two gated x-ray imagers [15,16] monitored the Ar *K*-shell emission from the microsphere, while neutron instruments measured the neutron time of flight and neutron yield of the D-D reactions [17].

A low-resolution survey spectrometer, having a resolving power $E/\Delta E$ of approximately 550, was used to record the Ar *K*-shell emission through a 390×500 μm^2 diagnostic slot centered at $\theta=90°$ and $\phi=104°$ and a high-resolution spectrometer, having a resolving power $E/\Delta E=1800$, was used for more detailed line-shape measurements through a 390-μm-diam diagnostic hole centered at $\theta=-169°$ and $\phi=-90°$. Where the hohlraum target axis is define as $\theta=90°$ and $\phi=0°$, with θ the polar angle and ϕ the azimuthal angle. The low-resolution instrument consists of a flat rubidium acid phthalate crystal coupled to an x-ray streak camera and aligned for a spectral range of 2.7–4.2 Å, which includes the Ar *K* shell. The spectrometer resolving power was limited by the spatial resolution of the x-ray streak camera, which has been measured as 150 μm in the central 15–20 mm of the camera, deteriorating to 400 μm towards the edges [18]. The estimated dispersion from the source-crystal-film geometry is 45 mÅ/mm. Higher spectral resolu-

tion was achieved using a second similar x-ray streak camera and pentaerythritol crystal by altering the spectrometer geometry to give a dispersion of 12.1 mÅ/mm; the dispersion is estimated from the source-crystal-film geometry. The primary use of this spectrometer was the detailed measurements of the Ar Heβ transition.

Both spectrometers were mounted on x-ray streak cameras, which were equipped with CsI photocathodes, 250-μm-wide temporal slits on a 0.5-mm-thick Ta substrate, and ITT image intensifiers [8]. The cameras were filtered with 635 μm of Be in front of the crystal and a 50-μm Be debris shield over the photocathodes. The temporal resolution of the streak cameras was estimated from the sweep speed, the slit widths, the camera magnification, and the spatial resolution. The temporal resolution was found to be 22.4 and 20.7 ps for the low- and high-resolution cameras, respectively, while the cameras have an approximate streak duration of ~ 2.5 ns [12].

The microsphere core was imaged with gated microchannel plate x-ray pinhole cameras, filtered to record x-ray emission above 3 keV, principally Ar K-shell emission. One camera observed the microsphere at a magnification of 8 through a 390-μm-diam diagnostic hole centered at $\theta = -108°$ and $\phi = -90°$. This camera was equipped with four active strips: Each strip records four images of the microsphere through 10-μm-diam pinholes, with an approximate gate time of 70 ps per pinhole and image-to-image delay of 80 ps [9]. The second camera was aligned to record the microsphere through a LEH, viewing along the axis of the hohlraum target. This camera was equipped with a single continuous serpentine strip recording 12 images at a magnification of 3 through 15-μm-diam pinholes [10]. The imaging cameras were filtered with 550 μm of Be with an additional 50 μm of Be as a debris shield protecting the microchannel plates. X-ray data from all the cameras were recorded on Kodak TMX-3200 film and each piece of film was calibrated against a standard.

B. Data reduction

In overview, data reduction consists of (i) digitizing the film; (ii) converting the digitized data from film density to exposure; (iii) removing instrument effects such as distortion; (iv) determining the spectral dispersion (Å/mm) and time axis (ps/mm); (v) applying corrections for filter transmission, photocathode efficiency, and crystal reflectivity; and, finally, reducing the data to the instrument resolution while extracting cross sections along the wavelength direction for analysis.

In more detail, data recorded on film were digitized with a 12-bit digitizing system [19] typically at 60-μm spatial resolution with matching slits in the xy plane. The conversion of film density to exposure ($D - \log_{10} E$ curve) was derived from an absolutely calibrated density wedge that is exposed onto the same film and processed with the data. Using the $D - \log_{10} E$ curve, the digitized film density data was converted to exposure and then corrections for instrument distortion were applied. The goal of this part of the data reduction is to ensure that the spectral direction and the temporal direction are straight and orthogonal. To achieve this we assume that the gold spectral lines should be straight, which defines the spectral direction, and that the continuum from the imploding microsphere arises at the same time for all spectral components, which defines the temporal direction. The relative time delay due to the fact that different paths are transverse for different wavelengths is small, i.e., less than 22 ps for the survey spectrometer and less than 7 ps for the high-resolution spectrometer. Using image analysis software [20], three to four of the resolved Au spectral lines are separately traced and fitted to a polynomial. Distortion was removed by straightening the polynomials and linearly interpolating between the fitted traces. Points outside the fitted traces are corrected by linear extrapolation. The distortion-corrected image was recovered by shifting the pixels according to this prescription. This produced data with orthogonal time and space axes. Next the image was rotated to ensure that the axes were horizontal and vertical before any analysis can be made. The orientation was determined by ensuring that the gold spectral lines are horizontal in the digitized image. Rotations were performed by a pixel shift technique.

Now the dispersion, that is, the energy or wavelength versus distance on the film relationship, is fitted to the data. The dispersion was estimated from the spectrometer geometry and confirmed by matching the well-documented Ar K-shell resonance lines [21] to the principle spectral features in the streak camera records. Thus the dispersion of the survey spectrometer was accurately determined. Then, using this dispersion we identify several Au M-band spectral lines that are emitted from the hohlraum target wall in the spectral vicinity of the Ar Heβ transition. The same Au M-band lines are then identified in the high-resolution spectra, thus allowing the dispersion of the high-resolution spectrometer to be confirmed. Once the dispersion is determined, corrections for the filter transmission [22], photocathode response [23], and crystal integrated reflectivities [22] are removed from the image by division. We note that these intensity corrections are small over any of the spectral features and do not introduce any significant errors. The final stage before analysis is to reduce the data to the camera resolution by averaging along the wavelength direction and then extracting cross sections in this direction.

C. Data analysis

The spectroscopic data are analyzed by comparing line-shape measurements of the Ar Heβ transition to calculations that include the Li-like autoionizing satellites $2l3l'$ and $3l3l'$. This approach has become possible only recently whereby data are compared to a line-shape database calculated over a T_e and n_e grid using TOTAL [24] and nonlocal-thermal-equilibrium (NLTE) populations. The best comparison between experiment and calculated line shape gives spatially averaged T_e and n_e. In the past, due to the high computational costs, such analysis has been applied to single cross sections; here we apply the technique for all times in the streak camera records.

Since Au M-band continuum emission from the imploding microsphere and general background contaminates the Ar K-shell spectra, which all vary with time, each spectral cross section is individually analyzed. Careful background and continuum removal is essential to ensure reliable and reproducible analysis. The survey and the high-resolution

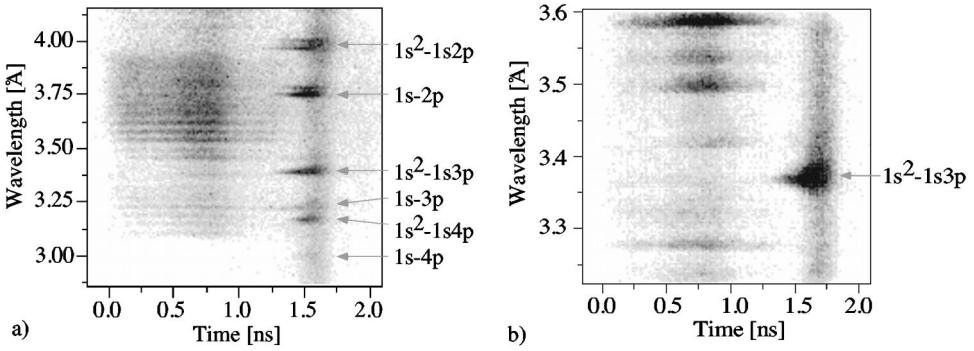

FIG. 2. Time-resolved spectroscopic data from a D_2/Ar- filled (50/0.1 atm) microsphere imploded with 19 kJ: (a) survey spectra and (b) high-resolution spectra. Au M-band emission is observed for the first nanosecond. The Ar K-shell emission starts at $t \approx 1.25$ ns. The Ar K-shell features are identified.

Heβ data are prepared by fitting a low-order polynomial to data between 3.2 and 3.6 Å and interpolated under the Ar Heβ line shape while excluding other spectral features. The data, with the background removed, are compared with the TOTAL database. An efficient comparison is possible using a distributed computer environment developed by Nash *et al.* [25], which allows line-shape databases to be accessed rapidly and interpolated in an interactive fashion. Using this environment, a plasma temperature and density are selected and the theoretical line shape is extracted, interpolated to the correct plasma conditions, and convolved with a Gaussian profile representing the instrument broadening function before comparing with data. T_e is determined by matching the relative intensity of the Ar Heβ peak and the Li-like $2l3l'$ and $3l3l'$ satellites and n_e is determined by matching the shape of the high-energy side of the Ar Heβ line. This process is graphically illustrated Ref. [3].

In some cases we have analyzed the spectroscopic data with a second method. The second method is based on fitting the two K-shell $n=1$ to 3 resonances and using the integrated line intensities ratios to determine a T_e and the FWHM to extract n_e [26]; data are compared to predictions from the collisional radiative kinetics code FLY [27] to give T_e and n_e. This second method represents a more classical method of plasma spectroscopic analysis [26]. A polynomial fit is made to the cross sections taken through the survey spectra between 3.0 and 3.6 Å, while Gaussians are fitted to the Ar Heβ and Ar Lyβ transitions. Spectral features, such as Au M-band lines, are excluded. In addition, the Gaussian fitting is restricted to the peak and the high-energy side of the Ar Heβ transition to exclude the Li-like dielectronic satellites and to the high-energy side of Ar Lyβ to exclude the Ar Heγ, $n=1-4$ transition that appears on the low-energy side of the Ar Lyβ line shape. This analysis, corrected for the instrument broadening, is repeated for each cross section to derive T_e and n_e time histories. The n_e diagnostic is insensitive to T_e and is robust as the FWHM is proportional to $n_e^{2/3}$. Further, ion dynamics do not affect the linewidths of these transitions [1]; however, as the line ratio is sensitive to the ionization populations, an n_e dependence in the determination of T_e must be accounted for.

III. EXPERIMENTAL RESULTS

In this section spectroscopic data obtained from the implosion experiments are presented. The implosion of D_2-filled microspheres is described first. Core T_e and n_e time histories are spectroscopically determined. We show first that the spectroscopic data are reliable by comparing, where possible, these results with measurements derived from other diagnostics and second that the implosion experiments are reproducible by demonstrating small experiment-to-experiment variation. We then compare these results with implosion spectra from a series of experiments where the gas fill is varied. Here we study Ar doped in D_2, CD_4, N_2, and Ne fills. Gas-fill pressures were adjusted to ensure that the total number of electrons in the core remained fixed between the experiments; the gas fills are summarized in Table I.

A. Implosion of deuterium-filled microspheres

Examples of Ar K-shell emission survey spectra between 2.9 and 4.1 Å and high-resolution spectra between 3.2 and 3.6 Å from indirectly driven implosions of D_2 filled microspheres are displayed in Figs. 2(a) and 2(b), respectively [2,3]. The spectral dispersion is along the vertical axis with time increasing left to right; $t=0$ ns was determined from the data and is found, *a posteri*, to indicate the time the laser first strikes the hohlraum target. The Ar K-shell emission features, i.e., $n=1-2$ (Heα and Lyα), $n=1-3$ (Heβ and Lyβ), and $n=1-4$ (Heγ and Lyγ), are identified. The spectra have been corrected for crystal, filter, photocathode, streak camera, and film effects as described.

Figure 2 shows that bright Au M-band emission is emitted for the first nanosecond while the laser irradiates the hohlraum target interior and the M-band features decay when the laser is turned off. By $t \approx 1.25$ ns Ar K-shell emission is observed and the K-shell emission intensity increases as the implosion proceeds. The Ar Heβ emission intensity peaks at 1.6 ns, remains high for a further 0.1 ns, and then falls rapidly; after 1.8 ns the continuum is dominant and the Ar K shell is not visible. Between $t \approx 1.5$ and 1.75 ns Ar K-shell spectra are superimposed on bright continuum emission from the converging shell. The relative intensities of the Ar K-shell features indicate that the ionization balance during the implosion is approximately 50% He-like.

During the implosion the Ar Heβ and Ar Lyβ transitions are Stark broadened. The narrowest, instrument-limited linewidths are measured at 1.25 ns; the linewidth broadens to a maximum width of approximately 30 eV at 1.7 ns. After 1.7 ns the lines begin to narrow again. However, the signal-to-noise level drops after 1.7 ns, complicating the linewidth

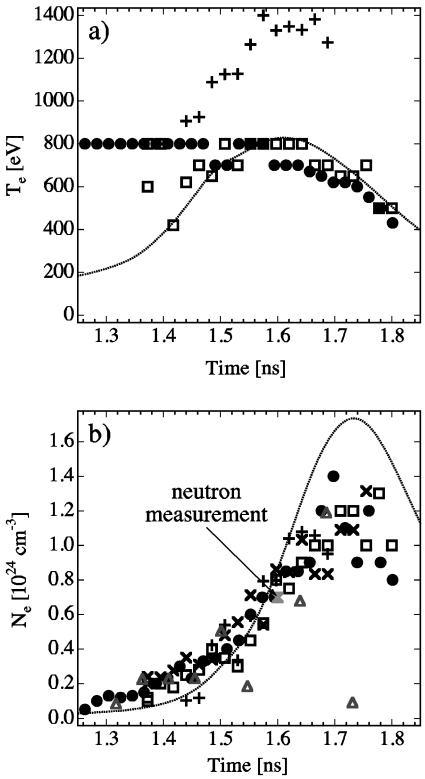

FIG. 3. (a) $T_e(t)$ and (b) $n_e(t)$ extracted from the data shown in Fig. 2. ●, line-shape fits to the high-resolution spectra; ■, line shape fits to survey spectra; +, line intensity ratios in the upper graph and Lyβ FWHM in the lower graph; ×, Heβ FWHM;——, mass-averaged simulations; ▲, gated x-ray imager results.

measurements. During the implosion the Ar Heβ line shape is seen to broaden symmetrically; this is confirmed in Fig. 2(b), where the Ar Heβ transition has been recorded at higher resolution.

The data in Figs. 2(a) and 2(b) have been analyzed to give spatially averaged T_e and n_e time histories. Figure 3(a) shows T_e estimated using Ar Heβ line-shape fits to the high-resolution spectra (closed circles), Ar Heβ line-shape fits to survey spectra (open squares), and line intensity ratios (crosses). There are significant differences between the two techniques with the line intensity ratios predicting a higher T_e; this is discussed in Sec. V. In Fig. 3(b) n_e time histories from Ar Heβ line-shape fits to the high-resolution spectra (closed circles), Ar Heβ line-shape fits to survey spectra (open squares), FWHM measurements of the Ar Heβ (crosses), and FWHM measurements of the Ar Lyβ (pluses) survey spectra are shown. To verify the mapping of the time-dependent spectra to $n_e(t)$ we compare the results to $n_e(t)$ extracted from x-ray imaging data of the core. To do this we assume that the gas fill is ionized and the image represents the core diameter; the results are shown as open triangles in Fig. 3(b). The latter assumption breaks down as the microsphere assembles at $t \approx 1.7$ ns due to a bright continuum and a drop in Ar K-shell emission. The spectroscopic determined n_e are also supported by the neutron measurements, which give a ρR of ~ 6 mg/cm^2, leading to an n_e of 7×10^{23} cm^{-3} at peak T_e; this data point is indicated in the figure. The data in Fig. 3 are compared with the mass-averaged results from one-dimensional simulations (solid line); the simulations are discussed in Secs. IV and V.

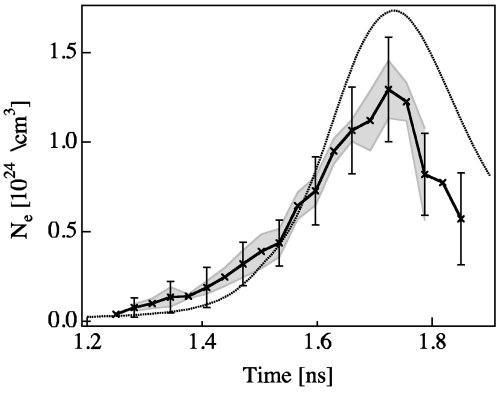

FIG. 4. n_e time histories from five similar implosions represented by the solid line. The shaded region is the rms experiment-to-experiment variation and error bars are the estimated accuracy. The mass-averaged simulated n_e is the dotted line.

Further, the reproducibility of the experiments and the data analysis is investigated by comparing T_e and n_e from five similar experiments. In Fig. 4 $n_e(t)$ from these experiments are shown: The solid line represents the mean $n_e(t)$ and the shaded region the root-mean-square (rms) deviation. Again the time history is compared with simulation, as will be discussed below. The error bars represent the estimated error in determining n_e. The results illustrate a small experiment-to-experiment variation. Care was taken to ensure that the targets were similar and the laser energy was 19 ± 2 kJ in the experiments. An independent indication of the reproducibility of the experiments is the small variation in the D-D neutron yield, which was $(4 \pm 2) \times 10^8$.

B. Gas fill study

To access the hydrodynamic performance and the potential of using higher $\langle Z \rangle$ gas cores as a high-density spectroscopic source experiments replacing the deuterium gas fill with CD_4, N_2, or Ne were undertaken. The results are shown in Figs. 5 and 6. Figures 5(a) and 5(b) show, respectively, corrected time-resolved Ar K-shell survey spectra and high-resolution Ar Heβ spectra from imploded CD_4-filled microspheres. The time-resolved spectra show the familiar Au M-band emission from the hohlraum target for the first nanosecond. The emission decays when the laser turns off. Ar K-shell emission is observed at $t \approx 1.3$ ns. The K-shell spectra intensity increases with peak Ar Heβ emission occurring at $t \approx 1.6$ ns. The Ar Heβ line broadens due to the Stark effect as the core is compressed and approaches the maximum linewidth at 1.6 ns, i.e., the peak core density is achieved at 1.6 ns. Target disassembly follows; during this phase the K-shell intensity including the Ar Heβ emission rapidly decreases. The spectra become continuum dominated until 1.8 ns.

The CD_4 data can be compared with the D_2 results shown in Fig. 2. The data appear similar in some respects; however, the differences are marked and important. The CD_4 experiments lead to Ar emission spectra that is less intense compared to the continuum and the K-shell emission abruptly decays as the continuum emission increases at 1.6 ns. Thus, relative to maximum compression, which we asso-

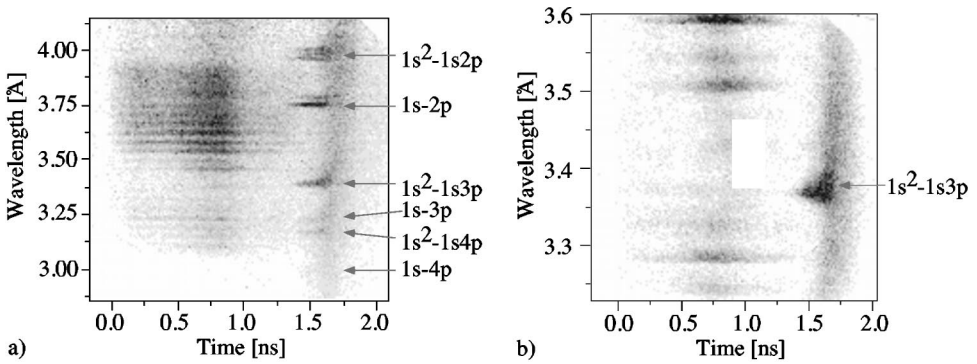

FIG. 5. Time-resolved spectroscopic data from CD_4/Ar-filled microsphere imploded with 19 kJ: (a) survey spectra and (b) high-resolution spectra. The Ar *K*-shell features are identified.

ciate with the broad continuum emission, occurs after peak emission, with no effective overlap. From the relative intensity of the spectral lines in *K*-shell spectra it is estimated that the ionization balance has shifted towards He-like, suggesting lower average temperatures during the implosion. Detailed analysis and simulation, discussed below, support this conclusion. We also find that the measurement of the Ar Heβ transition indicates that the line shapes are asymmetric. The asymmetry increases with time as the line profile extends to a longer wavelength. This is particularly apparent in high-resolution measurements [Fig. 5(b)]. The asymmetry is associated with the relatively lower T_e as compared to the D_2 measurements. Lower T_e yields an increased Li-like population leading to Li-like dielectronic satellites. The satellites modify the line profile, extending it to a longer wavelength.

We now consider the emission spectrum obtained during the implosion of the N_2- and Ne-filled microsphere. The spectroscopic results, from the survey instrument, are shown in Figs. 6(a) and 6(b), respectively, and are significantly different from the results shown in Figs. 2(a) and 5(a). Figure 6(a) shows intense Ar *K*-shell emission between 1.2 and 1.3 ns only. This and the continuum emission occur only as the leading shock propagates through the core, heating the core gases. Radiative cooling of the core is very efficient and during the next 0.1 ns Ar *K*-shell emission and continuum emission are notably absent. This is followed by intense continuum emission from $\sim$1.4 to 1.7 ns as the shell converges. The implosion of the Ne-filled microsphere [Fig. 6(b)] is more dramatic as Ar *K*-shell emission is not observed at any time during the implosion and continuum emission is only weakly observed at 1.7 ns. The data in Fig. 6(b) were obtained from an implosion of a neon-filled microsphere imploded with only 13 kJ of energy; we note that similar results are obtained from neon targets when imploded with energies between 11 and 32 kJ. Again, the most likely cause for the absence of an observable Ar *K* shell is the modification to the hydrodynamics due to radiative cooling. This will be discussed in Sec. IV.

In summary, the spectroscopic results show that the implosion hydrodynamics are significantly altered by changing the gas fill. In Sec. IV we explore the hydrodynamics of these implosions through simulation. One motivation for increasing the $\langle Z \rangle$ of the gas fill is to study the effects of ion dynamics on the Ar Heβ line shape.

C. Ion dynamics study

Ion dynamics effects may be important at the plasma conditions reached in high-energy-density implosions [1,5]. Detailed measurements of the Ar Heβ transition have been made to access these effects. Three cross sections taken close to peak compression of a D_2 core are shown in Fig. 7. The data were extracted from Fig. 2(b) at $t=1.53$, 1.64, and 1.74 ns. Each cross section is compared with a TOTAL calculation; the calculations include the Ar Heβ transition and the Li-like $2l3l'$ and $3l3l'$ satellites. The best agreement between experiment and calculation is found for $T_e=800$ eV and $n_e=4.5\times10^{23}$ cm^{-3}, $T_e=700$ eV and $n_e=8.5\times10^{23}$ cm^{-3}, and $T_e=600$ eV and $n_e=9\times10^{23}$ cm^{-3}, respectively. The comparison clearly demonstrates that the intensity dip at the

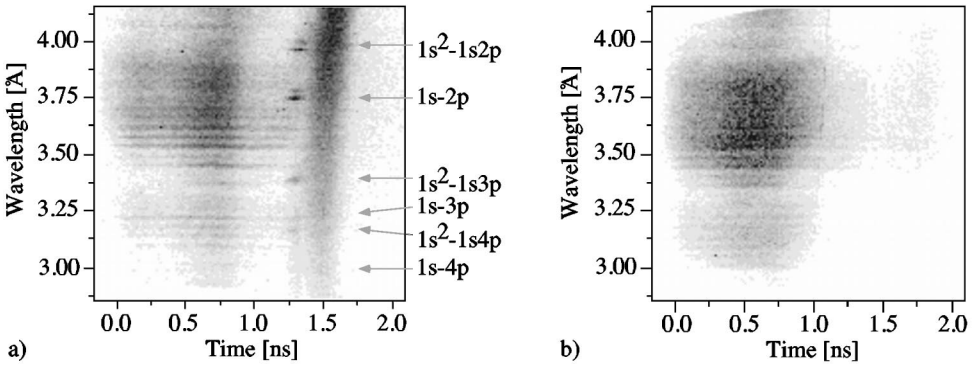

FIG. 6. Time-resolved spectroscopic data from (a) N_2/Ar-filled microsphere imploded with 18 kJ and (b) Ne/Ar-filled microsphere imploded with 13 kJ. Note that the Au *M*-band emission is observed during the first nanosecond.

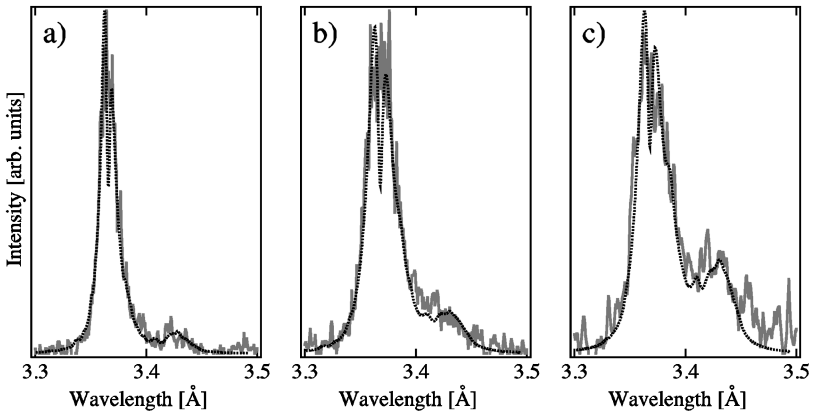

FIG. 7. High-resolution Ar Heβ line-shape measurements (solid line) from the D_2/Ar-filled microsphere compared to TOTAL calculations (dashed line). (a) $t=1.53$ ns, calculation of $T_e=800$ eV and $n_e=4.5\times10^{23}$ cm^{-3}; (b) $t=1.64$ ns, calculation of $T_e=700$ eV and $n_e=8.5\times10^{23}$ cm^{-3}; and (c) $t=1.74$ ns, calculation of $T_e=600$ eV and $n_e=9\times10^{23}$ cm^{-3}. Note that the intensity dip at the line center is *not* observed.

line center is not observed during the implosion. Calculation indicates that the peak-to-peak separation about the intensity dip of 6.5, 10, and 9.8 mÅ, respectively, should be observable. The high-resolution spectrometer resolution is approximately 1.7 mÅ and an upper limit to Doppler broadening of 2 mÅ is calculated, assuming a central core ion temperature of 2 keV. The data shown in Fig. 7 show that the Li-like satellites are relatively small due to the high T_e, so that these satellites do not modify the central portion of the line profile. This is supported by hydrodynamic simulations, discussed below, which indicate that T_e is above 600 eV and the T_e spatial gradients are small after $t\approx1.5$ ns. Note that an Ar Heβ line-center shift of approximately 2.2 mÅ was accounted for during the data analysis. This is derived from times of low electron density, so that this *apparent* shift is due to diagnostic effects, data correction procedures described earlier, or finally inaccurate base-line atomic data. Indeed, there are no absolute wavelength fiducials, and within experimental accuracy absolute line shifts of this order cannot be confirmed.

In a previous article [1] we indicated that measured Ar Heβ line profiles are more accurately reproduced if ion dynamics are included in the line-shape calculations. However, this is not a definitive test of ion dynamic effects at high-energy density. To conclusively demonstrate ion dynamic effects we have replaced the D_2 gas fill with gases of higher molecular (i.e., atomic) mass. The increase in mass slows the motion of the perturbing ions and the rate of fluctuation of the ion microfield. Experiments show that this approach leads to enhanced radiative cooling of the implosion resulting in significant modification of the core hydrodynamics. Radiative cooling leads to a loss of Ar K-shell emission intensity. Simulation has confirmed that the core hydrodynamics are altered, increasing the temporal mismatch between peak T_e and peak n_e. Simulation also indicates that T_e and n_e spatial gradients increase. However, K-shell emission spectra were obtained from the CD_4-filled microspheres; it is possible that the effects of ion dynamics may be seen in this data [1]. Three spectral cross sections taken from Fig. 5(b) are shown in Fig. 8 and correspond to times $t=1.40$, 1.52, and 1.65 ns. The continuum and background have been removed; the emission intensities are arbitrary. The noise in the line shapes is due to the bright continuum levels in the data. Again, these line-shape measurements do not show the predicted intensity dip at the line center. We note that the hydrodynamics are different to the D_2 case: The spatial gradients are higher and the average T_e is lower. It is possible that the line profiles are modified by the strong Li-like satellite features on the low-energy wing of the Heβ transition, as

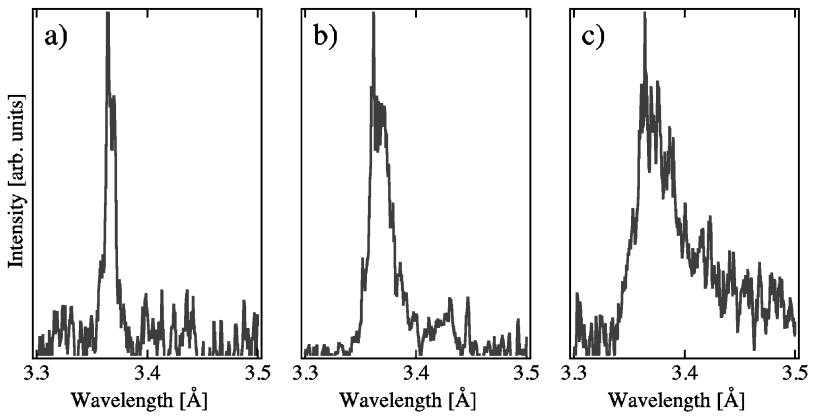

FIG. 8. High-resolution Ar Heβ line-shape measurements from CD_4/Ar-filled microsphere. (a) $t=1.40$ ns, (b) $t=1.52$ ns, and (c) 1.65 ns.

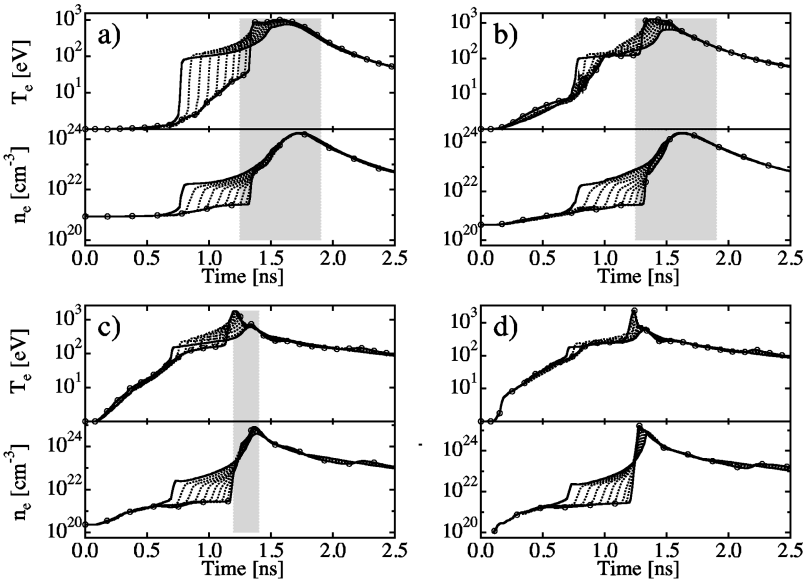

FIG. 9. HYADES implosion simulations of (a) D_2/Ar-, (b) CD_4/Ar-, (c) N_2/Ar-, and (d) Ne/Ar-filled microspheres. The upper graph shows the simulated $T_e(t)$ and the lower graph the simulated $n_e(t)$. The time histories for ten Lagrangian points within the core of the microsphere are shown. The shaded region indicates the time over which experimental Ar *K*-shell emission is observed in Figs. 2, 5, 6(a), and 6(b), respectively. The outermost core is represented by the solid line and the innermost core by the solid line and circles.

indicated by the line-shape asymmetry, masking an intensity dip at the line center. These plasmas are explored further by hydrodynamic simulation in the following section.

IV. HYDRODYNAMIC MODELING

Understanding the formation of dense plasma cores in an imploding microsphere can be enhanced by computer simulation; however, these simulations must be used as a benchmark to be compared against reliable, reproducible, and accurate experimental data. Comparisons between experiment and one-dimensional simulation are shown in Fig. 3 and demonstrate broad agreement. In this section we describe the one-dimensional simulations. The motivation has been to keep the simulations simple while ensuring that the essential physics of an indirectly driven implosion were included. Thus we have used a single temperature Planckian radiation source to drive the implosion and an ideal gas equation of state. Simulations of the D_2 microsphere are shown in Fig. 9(a). Here ten Lagrangian zones in the core are displayed and upper curves show the evolution of T_e with time and lower curves show n_e. The time histories of the outermost and innermost cores are shown by the solid line and circles, respectively. The shaded region indicates the times that the Ar *K*-shell emission was experimentally observed. The hydrodynamic model is modified to simulate the implosion of CD_4-, N_2-, and Ne-filled microspheres; the results are shown in Figs. 9(b), 9(c), and 9(d) simulations, respectively. We describe the hydrodynamic model first and then present the D_2 simulations and finally the gas fill results.

A. Computer model

We model the experiments with HYADES [28] a commercially available one-dimensional Lagrangian radiation-hydrodynamics computer code. The energy and mass transport equations were solved in spherical geometry with energy coupled into the microsphere using a Planckian radiation spectrum. The time-dependent Planckian temperature T_r was measured from an empty hohlraum target irradiated with 16 kJ of laser energy in a 1-ns square laser pulse and measured using a filtered ten x-ray diode array [29]. We model the microsphere with NLTE screened hydrogenic average-atom atomic physics and treat radiation transport in the multigroup flux-limited diffusion approximation. The energy exchange between the electron and ion fluids occurs through electron-ion coupling with ion and electron flux-limited diffusion. Pressures, energies, and thermodynamic properties of the microsphere (i.e., core and shell) were derived from an ideal gas equation of state (EOS). The initial electron, ion, and radiation temperatures were set to 1 eV and the minimum ionization temperature was 5 eV. Cold opacities were assumed for temperatures below 20 eV. Steady-state NLTE was assumed for temperatures up to 50 eV; above 50 eV time-dependent NLTE was used. Flux-limited electron and ion thermal conductivities were used with flux limiters of 0.05 and 0.4, respectively.

The simulated microsphere was identical to the nominal experimental target illustrated in Fig. 1(b) and described in more detail in Tables I and II. The target is simulated with 50 zones in the core and 8, 3, and 16 zones for the polystyrene, PVA, and parylene-N layers of the shell, respectively. The layer interfaces were mass matched, with the inner most zone containing 3% of the core mass.

B. Simulation of deuterium-filled microspheres

The simulation is driven by a time-dependent Planckian x-ray source [3] incident on the outer shell of the microsphere. Energy is coupled into the shell principally through ionization and is transported inward by electron thermal conduction; the ions are then collisionally heated [30]. As the heated exterior of the plastic shell expands a shock forms. In addition, material ablation from the shell surface accelerates the interior inward. Energy is continuously deposited into the

accelerating shell resulting in further ablation and a piston-like compression. Figure 9(a) shows T_e (upper curves) and n_e (lower curves) in the core of a D_2-filled microsphere. Initially, T_e and n_e increase slowly until about 0.5 ns; this results from the long electron mean free path (mfp), which leads to preheating of the interior and, to a lesser extent, absorption of radiation. At approximately 0.75 ns the shock enters the core and a jump in T_e and n_e occurs. As the shock propagates through the core it converges, increasing in strength, which leads to the increase in the T_e jump as the shock approaches the core center. The shock consists of two components, one due to the electrons and the large electron mfp and the other due to the ions with a short mfp [31,32]. The long electron mfp enables energy transport ahead of the ion component of the shock. Shock momentum transport is due mainly to the ions. As T_i exceeds T_e an increase in T_e occurs after the passage of the shock; T_i and T_e equilibrate through (weak) electron-ion coupling, i.e., collisions. The temperature continues to rise as energy from the drive is deposited into the microsphere and the compression of the core continues through the inward motion of the massive shell. The shock converges on the core center and T_e peaks to 870 eV at 1.37 ns, dropping slightly as the shock unloads. T_e peaks again at 1.55 ns and again at 1.6 ns as the shock reflects between the core center and the incoming material. After 1.6 ns T_e falls monotonically. It should be noted that the T_e remains above 700 eV between 1.35 and 1.75 ns. In comparison, the peak ion temperatures are high and exceed 2 keV as the shock converges; the core T_e rapidly attains T_i as the density rise increases the electron-ion collision rate.

The lower graph in Fig. 9(a) indicates that the compression of the core lags the increase in T_e. The compression continues to increase as the shell converges even while the core center cools; the peak n_e of 1.8×10^{24} cm^{-3} occurs at 1.74 ns in the core center, approximately 0.15 ns after peak T_e. At this time $T_e\approx750$ eV. During the period before peak compression the inward motion of the shell is decelerated as the pressure in the core rises; stagnation occurs at 1.74 ns and is followed by disassembly. The simulated T_e and n_e spatial gradients are small after the initial shock compression and the global peak T_e occurs at the core center while the global peak n_e occurs in the outer core.

C. Simulation of CD_4-N_2-and Ne-filled microspheres

Figures 9(b), 9(c), and 9(d) show simulation results for CD_4-, N_2-, and Ne-filled cores, respectively. The simulations illustrate the effects of altering the gas fill on the hydrodynamics; changing the fill gas increases the total mass of the core and the average atomic number $\langle Z\rangle$. Of particular importance to the hydrodynamics is the higher $\langle Z\rangle$, which leads to an increase in the ionization energy [33] and an increase in the electron-ion collision cross sections [34] and reduced ion and electron MFPs. The core opacity and reemission of radiation also increase [26,30]. These factors result in an increased shock strength, causing a more rapid implosion with concomitant higher peak temperatures and densities in the core. This is especially apparent in the N_2 and Ne simulations in Figs. 9(c) and 9(d). The deuterium simulation [Fig. 9(a)] shows n_e peaks in the outer core, while both T_e and n_e peak at the core center for higher $\langle Z\rangle$ targets as seen in Figs. 9(b)–(d). Again this is a direct result of very strong shock compression. We also find that the spatial gradients $T_e(r)$ and $n_e(r)$ are more significant as $\langle Z\rangle$ increases.

In more detail, as $\langle Z\rangle$ increases we find that the drive radiation and reemitted radiation are more effectively absorbed by the core gases. This results in considerable core preheating. Initially, this is not apparent and n_e remains low due to high ionization energies. After approximately 0.15 ns n_e increases. Preheating of the core is followed by a shock that enters the core at approximately 0.75 ns (approximately the same time in all simulations). The T_e (and T_i) jump associated with the shock increases with $\langle Z\rangle$ as a result of the decreased ion mfp and higher viscosity. The shock is further strengthened by more efficient absorption of radiation. Due to core preheating and the high shock strength, the shock velocity is greater, resulting in an implosion that occurs more rapidly. Extremely high electron and ion temperatures may be reached during shock convergence, i.e., $T_e\sim2000$ eV and $T_i\sim30$ keV for the N_2 simulation, but due to the high collision rate a steady state is rapidly attained. However, radiative losses continue to promote rapid cooling of the core center. During the temperature drop the density at core center also decreases; however, the density drop is less severe as the inward motion of the shell maintains the compression. Indeed, T_e and n_e continue to increase in the outer core regions, while a significant drop in T_e and n_e at the core center is predicted. Stagnation occurs as the core pressure rises and decelerates the shell; this occurs at $t\approx1.4$ ns for N_2 and Ne [see Figs. 9(c) and 9(d)] compared to $t\approx1.7$ for D_2 [see fig. 9(a)] and $t\approx1.6$ for CD_4 [see Fig. 9(b)]. Microsphere disassembly appears to be determined by the mass of the shell and is similar for all simulations.

The simulations indicate that the implosion of deuterium-filled microspheres leads to a high-energy-density plasma with relatively small T_e and n_e spatial gradients. As the average Z of the fill gas is increased, radiative processes start to dominate the implosion hydrodynamics increasing the temporal delay between peak T_e and peak n_e and leading to strong gradients. In the following section we discuss the implication of these simulations on the interpretation of the spectroscopic data.

V. DISCUSSION

High-quality, time-resolved, spectroscopic data from an inertially confined plasma have been analyzed to give reliable, reproducible, and accurate time histories of the core plasma conditions. Time resolutions of approximately 25 ps were achieved and sophisticated line-shape data analysis techniques were implemented to derive $T_e(t)$ and $n_e(t)$ independently of the core hydrodynamics. The time histories were compared, where possible, with independent diagnostics and by cross comparing results from different spectrometers we have shown that the implosions are accurately diagnosed. Indeed, a series of similar experiments have shown that these implosion experiments are reliable and reproducible. The time histories have been compared with radiation-hydrodynamic simulations.

The T_e diagnostic is derived from the ratio of the Ar Heβ to Li-like satellite intensities. We find, however, that the diagnostic is useful only between 400 and 800 eV; below 400

eV the Li-like satellites dominate the line shape and a ratio cannot be determined; above 800 eV the Li-like populations are small and the Li-like contribution to the line profile cannot be distinguished from the background continuum. Typical sensitivities at 400 and 800 eV are ± 20 and ± 100 eV, respectively. With this in mind, T_e derived from the Ar Heβ line shape at times between 1.45 and 1.7 ns should be viewed as a lower-limit. In comparison, the n_e, where only the peak and high-energy side of the Ar Heβ transition were used in the fits, are accurately determined and the width is independent of temperature effects, e.g., ion dynamics.

Estimates of the T_e and n_e were also extracted using the integrated line intensity ratios and FWHM measurements of the *K*-shell 1-3 transitions, respectively. These results are compared in Figs. 3(a) and 3(b) with the line-shape method. We find that the integrated line intensity ratios lead to higher T_e estimates at all times. Hydrodynamic simulations support the lower T_e determined from the Heβ line profile. Keane *et al.* [35] have suggested that reabsorption of the optically thick 1-2 resonances (i.e., Ar Heα and Ar Lyα) in the outer core region may move the ionization balance towards the hydrogenic species. This optical depth would effect the *K*-shell 1-3 transition ratio measurement resulting in the diagnosed T_e being too high. To address this point the line intensity ratio diagnostic has been tested by calculating synthetic *K*-shell spectra using a collisional radiative kinetics code coupled to a hydrodynamic simulation package that includes radiative transfer and then comparing the complete *K*-shell spectra with experiment [35]. In contrast, the n_e derived by the two methods are in excellent agreement.

The experimental time histories for T_e and n_e were obtained using methods that are hydrodynamic independent and are compared to simulated mass-averaged T_e and n_e time histories of an imploding deuterium core by the solid lines in Figs. 3 and 4. The comparisons show that the simulations broadly reproduce the experimental results and that the one-dimensional radiation-hydrodynamic simulations are, in this sense, reasonable. We therefore conclude that the rudimentary physics of an indirectly driven implosion are approximated by the simulation. We see that small T_e and n_e spatial gradients are predicted, e.g.; see Fig. 9(a). Therefore, the experimental results must be considered as spatially averaged results. However, FLY calculations of *K*-shell spectra integrated across these predicted gradients show that they do not observably effect the optically thin Ar Heβ line profile, suggesting that a D_2 core is a suitable spectroscopic source [3,36]. We note that the Li-like $2l3l'$ and $3l3l'$ satellites were not included in these synthetic spectra.

It is important to note that these simulations were not exhaustive and important issues such as the accuracy of the EOS and the effects of frequency-dependent radiation sources were not considered. However, by keeping the approximation scheme simple the simulations illustrate the modeling of the radiation-target interaction physics, the EOS, and radiation transport produces acceptable results and indicates that these experiments are broadly understood and thus have furthered the understanding of the core plasma. These implosions are three dimensional and hydrodynamic instabilities play a critical role that impedes the target performance inevitably limiting core convergence, peak temperatures, densities, neutron yields, etc. These effects are not modeled by the one-dimensional simulations.

The hydrodynamics of the convergence phase of the implosion were designed to be stable; the laser drive and microsphere construction ensures a stable in-flight aspect ratio [11] achieving modest ρR product of ~ 6 mg/cm^2. A simple, reproducible 1-ns square laser drive pulse was used to create the radiation source; the implosion of the microsphere is preceded by a strong shock followed by the inward convergence of the shell. This resulted in an implosion insensitive to accurate shock timing, a subject of research in current ICF design [11]. However, as a well-defined robust implosion these experiments provide an excellent testing ground for high-energy-density plasmas.

The implosion of CD_4-, N_2-, and Ne-filled microspheres was investigated using the experimental, diagnostic, and simulation techniques developed for the D_2 experiments. Spectroscopic data were obtained; however, enhanced radiative cooling due to the higher-*Z* core gases was found to severely affect the visibility of the Ar *K* shell as the implosion hydrodynamics are modified. The CD_4 experiments produced analyzable spectra, whereas Ar *K*-shell emission was recorded during the initial shock compression of the N_2-filled microsphere, with no emission measured from the Ne experiments. The CD_4 data indicate that the average temperatures during compression are lower than those obtained with D_2 gas fills: In addition, simulation indicates that the T_e spatial gradients are more significant.

In general, we find that the theoretical line profiles reproduce the Heβ measurements, yet some features on the low-energy side of the Ar Heβ transition are not modeled. For example, experimental data show features at 3.18 and 3.26 Å and the wing intensity centered at 3.41 Å is higher than predicted. In addition, as peak compression is approached and during the disassembly of the core detailed structure appears in the line shape, which is not reproduced by the TOTAL calculations; cf. Fig. 7(c). Some of this structure exceeds the continuum intensity root mean square and is associated with a drop in T_e and an increased satellite contribution.

VI. CONCLUSIONS

Experimental and computational investigations of indirectly driven implosions have been described. High-energy-density deuterium plasmas have been shown to be reliably and reproducibly formed by indirectly imploding a plastic shelled microsphere with a radiation source created using 19 kJ of laser energy in a 1-ns square laser pulse. The principle diagnostic was the plasma spectroscopy of the Ar Heβ transition. These experiments were designed to ensure that the Ar Heβ transition remained visible and optically thin so that the line profile could be used to derive T_e and n_e time histories. Having achieved this, the experimental T_e and n_e time histories were extracted using techniques independent of the target hydrodynamics and were then compared with simulation.

The results of the comparison between the data and the simulations confirm that the one-dimensional radiation-hydrodynamic model broadly predicts the implosion of these targets. The simulations also indicate small spatial gradients in the imploding core, confirming that these plasmas are a

potentially useful spectroscopic test bed.

Detailed inspection of the Ar Heβ line profiles confirms that an intensity dip predicted by quasistatic ion spectral line shape calculations is not observed. The data indicate that the T_e is high enough to ensure that the Li-like populations are small, so the Li-like dielectronic satellites do not adversely effect the Heβ line center. Further, line shifts that may obscure the intensity dip are not observed. This suggests that the discrepancy at line center may be the result of ion dynamic effects; however, this is not conclusive as a combination of the effects discussed above could produce a similar result. Detailed consideration of the Ar Heβ line profiles also indicates structure on the low-energy wing of the Ar Heβ transition. This structure exceeds the rms noise in the data and is not fully reproduced by the line-shape calculations.

The existence of lower temperatures is confirmed by the presence of Li-like dielectronic satellites that lead to asymmetric Heβ line profiles. It is possible that the difficulty in matching experimental profiles with a single calculated line shape results from the integration of Heβ transitions over a range of T_e and n_e conditions in the core to form the experimental profile. Although one-dimensional simulations suggest that spatial gradients are negligible, small experimental measurements of the gradient structure are required to verify these simulated predictions.

ACKNOWLEDGMENTS

The authors acknowledge the expert assistance of Target Fabrication and the technical team at Nova. Part of this work was performed under the auspices of the U.S. Department of Energy at Lawrence Livermore National Laboratory under Contract No. W-7405-Eng-48.

[1] N. C. Woolsey, A. Asfaw, B. Hammel, C. Keane, C. A. Back, A. Calisti, C. Mossé, R. Stamm, B. Talin, J. S. Wark, R. W. Lee, and L. Klein, Phys. Rev. E **53**, 6396 (1996).

[2] N. C. Woolsey, B. A. Hammel, C. J. Keane, A. Asfaw, C. A. Back, J. C. Moreno, J. K. Nash, A. Calisti, C. Mossé, R. Stamm, B. Talin, L. Klein, and R. W. Lee, Phys. Rev. E **56**, 2314 (1997).

[3] N. C. Woolsey, B. A. Hammel, C. J. Keane, A. Asfaw, C. A. Back, J. C. Moreno, J. K. Nash, A. Calisti, C. Mossé, R. Stamm, B. Talin, C. Hooper, L. Klein, and R. W. Lee, J. Quant. Spectrosc. Radiat. Transf. **58**, 975 (1998).

[4] B. A. Hammel, C. J. Keane, M. D. Cable, D. R. Kania, J. D. Kilkenny, R. W. Lee, and R. Pasha, Phys. Rev. Lett. **70**, 1263 (1993); B. A. Hammel, C. J. Keane, T. R. Dittrich, D. R. Kania, J. D. Kilkenny, R. W. Lee, and W. K. Levedahl, J. Quant. Spectrosc. Radiat. Transf. **51**, 113 (1994).

[5] R. W. Lee, in *Atomic Processes in Plasmas*, edited by E. S. Marmar and J. L. Terry, AIP Conf. Proc. No. 257 (AIP, New York, 1991), p. 39.

[6] H. Griem, Phys. Fluids B **4**, 2346 (1992).

[7] A. Calisti, L. Godbert, R. Stamm, and B. Talin, J. Quant. Spectrosc. Radiat. Transf. **51**, 59 (1994); A. Calisti, L. Godbert, T. Meftah, C. Mossé, R. Stamm, and B. Talin, Laser Part. Beams **12**, 407 (1994); L. Godbert, A. Calisti, R. Stamm, B. Talin, R. W. Lee, and L. Klein, Phys. Rev. E **49**, 5644 (1994).

[8] C. F. Hooper, D. A. Haynes, D. T. Garber, R. C. Mancini, Y. T. Lee, K. Bradley, J. Delettrez, R. Epstein, and P. A. Jaanimagi, Laser Part. Beams **14**, 713 (1996); D. A. Haynes, Jr., D. T. Garber, C. F. Hooper Jr., R. C. Mancini, Y. T. Lee, D. K. Bradley, J. Delettrez, R. Epstein, and P. A. Jaanimagi, Phys. Rev. E **53**, 1042 (1996).

[9] I. N. Kosarev, C. Stehle, N. Feautrier, A. V. Demura, and V. S. Lisitsa, J. Phys. B **30**, 215 (1997).

[10] E. M. Campbell, Laser Part. Beams **9**, 209 (1991).

[11] J. Lindl, Phys. Plasmas **2**, 3933 (1995).

[12] R. W. Lee, R. Petrasso, and R. W. Falcone, Lawrence Livermore National Laboratory Report No. UCRL-ID-119170 (http://www.llnl.gov/science_on_lasers/), 1995 (unpublished).

[13] J. D. Kilkenny, Rev. Sci. Instrum. **63**, 4688 (1992).

[14] B. A. Hammel, P. Bell, C. J. Keane, R. W. Lee, and C. L. S. Lewis, Rev. Sci. Instrum. **61**, 2774 (1990).

[15] J. D. Kilkenny, P. M. Bell, B. A. Hammel, R. Hanks, O. Landen, T. McEwan, D. S. Montgomery, R. E. Turner, and J. D. Wieldwald, Proc. SPIE **1358**, 117 (1991).

[16] P. M. Bell, J. D. Kilkenny, G. Power, R. Bonner, and D. K. Bradley, Proc. SPIE **1155**, 430 (1990).

[17] M. D. Cable, S. P. Hatchett, and M. B. Nelson, Rev. Sci. Instrum. **63**, 4823 (1992); M. B. Nelson and M. D. Cable, *ibid.* **63**, 4874 (1992); R. A. Lerche, S. P. Hatchett, M. D. Cable, and M. B. Nelson, *ibid.* **63**, 4877 (1992); M. D. Cable, J. Appl. Phys. **60**, 3068 (1986).

[18] D. Kalantar, R. Costa, O. L. Landen, and T. Orzechowski; (private communication).

[19] Lawrence Livermore National Laboratory photodigitizing system (PDS).

[20] D. Phillion, LLNL software ''PDS Shrink'' for Macintosh 68K.

[21] R. L. Kelly, J. Phys. Chem. Ref. Data **16**, Suppl. 1, 1 (1987); J. H. Scofield, Lawrence Livermore National Laboratory Report No. UCID-16848, 1975 (unpublished).

[22] B. L. Henke, E. M. Gullikson, and J. C. Davis, At. Data Nucl. Data Tables **54**, 181 (1993).

[23] K. Premaratne, E. R. Dietz, and B. L. Henke, Nucl. Instrum. Methods Phys. Res. **207**, 467 (1983); B. L. Henke, J. P. Knauer, and K. Premaratne, J. Appl. Phys. **52**, 1509 (1981); B. L. Henke, in *Low Energy X-Ray Diagnostics*, edited by David T. Attwood and Burton L. Henke, AIP Conf. Proc. 75 (AIP, New York, 1981), p. 146.

[24] A. Calisti, F. Khelfaoui, R. Stamm, B. Talin, and R. W. Lee, Phys. Rev. A **42**, 5433 (1990).

[25] J. K. Nash, J. M. Salter, W. G. Eme, and R. W. Lee, Quant. Spectrosc. Radiat. Transf. **54**, 283 (1995).

[26] H. R. Griem, *Plasma Spectroscopy* (McGraw-Hill, New York, 1994).

[27] R. W. Lee and J. T. Larsen, J. Quant. Spectrosc. Radiat. Transf. **56**, 535 (1996); R. W. Lee, *ibid.* **40**, 560 (1988); R. W. Lee, B. L. Whitten, and R. E. Strout, *ibid.* **32**, 91 (1984).

[28] J. T. Larsen and S. Lane, J. Quant. Spectrosc. Radiat. Transf.

51, 179 (1994); J. T. Larsen, in *Radiative Properties of Hot Dense Matter*, Proceedings of the Fourth International Workshop, edited by W. Goldstein *et al.* (World Scientific, Singapore, 1991), p. 321; J. T. Larsen, Cascade Applied Sciences, Inc. Report No. CAS-010 1990 (unpublished).

[29] H. N. Kornblum, R. L Kaufman, and J. A. Smith, Rev. Sci. Instrum. **57**, 2179 (1986).

[30] R. More, in *Atomic and Molecular Physics of Controlled Nuclear Fusion*, edited by C. Joachain and D. E. Post (Plenum, New York, 1983).

[31] Ya. B. Zel'dovich and Yu. P. Raizor, *Physics of Shock Waves and High-Temperature Hydrodynamic Phenomena* (Academic, New York, 1966), Vol. 1.

[32] J. J. Duderstadt and G. A. Moses, *Inertial Confinement Fusion* (Wiley-Interscience, New York, 1982).

[33] C. Kittel, *Introduction to Solid State Physics*, 5th ed. (Wiley, New York, 1976).

[34] L. Spitzer, Jr., *Physics of Fully Ionized Gases*, 2nd ed. (Interscience, New York, 1967).

[35] C. J. Keane, B. A. Hammel, A. L. Osterheld, R. W. Lee, D. R. Kania, L. J. Suter, R. C. Mancini, C. F. Hooper, and N. D. Delamater, J. Quant. Spectrosc. Radiat. Transf. **51**, 147 (1994); C. J. Keane, B. A. Hammel, D. R. Kania, J. D. Kilkenny, R. W. Lee, A. L. Osterheld, L. J. Suter, R. C. Mancini, C. F. Hooper, and N. D. Delamater, Phys. Fluids B **5**, 3328 (1993).

[36] C. A. Back, N. C. Woolsey, A. Asfaw, S. H. Glenzer, B. A. Hammel, C. J. Keane, R. W. Lee, D. Liedahl, J. C. Moreno, J. K. Nash, A. L. Osterheld, A. Calisti, R. Stamm, B. Talin, L. Godbert, C. Mossé, S. Ferri, and L. Klein, *Spectral Line Shapes*, edited by M. Zoppi and L. Ulici, AIP Conf. Proc. No. 386 (American Institue of Physics, New York, 1997).